Multidimensionally constrained relativistic Hartree-Bogoliubov study of spontaneous nuclear fission

Zhao, Jie; Lu, Bing-Nan; Nikšić, Tamara; Vretenar, Dario

Multidimensionally constrained relativistic Hartree-Bogoliubov study of spontaneous nuclear fission

Jie Zhao (赵杰),[1,*] Bing-Nan Lu (吕炳楠),[2] Tamara Nikšić,[1] and Dario Vretenar[1]
[1]*Physics Department, Faculty of Science, University of Zagreb, Bijenicka 32, Zagreb 10000, Croatia*
[2]*Institut für Kernphysik, Institute for Advanced Simulation, and Jülich Center for Hadron Physics, Forschungszentrum Jülich, D-52425 Jülich, Germany*
(Received 22 October 2015; published 18 December 2015)

Background: Recent microscopic studies, based on the theoretical framework of nuclear energy density functionals, have analyzed dynamic (least action) and static (minimum energy) fission paths, and it has been shown that in addition to the important role played by nonaxial and/or octupole collective degrees of freedom, fission paths crucially depend on the approximations adopted in calculating the collective inertia.
Purpose: To analyze effects of triaxial and octupole deformations, as well as approximations to the collective inertia, on the symmetric and asymmetric spontaneous fission dynamics, and compare with results of recent studies based on the self-consistent Hartree-Fock-Bogoliubov (HFB) method.
Methods: Deformation energy surfaces, collective potentials, and perturbative and nonperturbative cranking collective inertia tensors are calculated using the multidimensionally-constrained relativistic Hartree-Bogoliubov (MDC-RHB) model, with the energy density functionals PC-PK1 and DD-PC1. Pairing correlations are treated in the Bogoliubov approximation using a separable pairing force of finite range. The least-action principle is employed to determine dynamic spontaneous fission paths.
Results: The dynamics of spontaneous fission of ^{264}Fm and ^{250}Fm is explored. The fission paths, action integrals, and the corresponding half-lives predicted by the functionals PC-PK1 and DD-PC1 are compared and, in the case of ^{264}Fm, discussed in relation with recent results obtained using the HFB model based on the Skyrme functional SkM* and a density dependent mixed pairing interaction.
Conclusions: The inclusion of nonaxial quadrupole and octupole shape degrees of freedom is essential for a quantitative analysis of fission dynamics. The action integrals and, consequently, the half-lives crucially depend on the approximation used to calculate the effective collective inertia along the fission path. The perturbative cranking approach underestimates the effects of structural changes at the level crossings and the resulting collective inertia varies relatively smoothly in the (β_{20},β_{22}) and (β_{20},β_{30}) planes. In contrast, the nonperturbative collective mass is characterized by the occurrence of sharp peaks on the surface of collective coordinates, that can be related to single-particle level crossings near the Fermi surface. This enhances the effective inertia, increases the values of the action integral, and results in longer fission half-lives.

DOI: 10.1103/PhysRevC.92.064315 PACS number(s): 21.60.Jz, 24.75.+i, 25.85.Ca, 27.90.+b

I. INTRODUCTION

Spontaneous fission (SF) presents a complex quantum process of evolution of a nucleus from the initial ground state to the final state with two fragments, and includes tunneling through barrier(s) in a multidimensional collective space [1]. A number of microscopic approaches, such as the time-dependent generator coordinate method (TDGCM) [2–6], the adiabatic time-dependent Hartree-Fock (ATDHF) or Hartree-Fock-Bogoliubov (ATDHFB) approximation [7–10], and mean-field instantons [11,12], have been developed to describe fission. However, the development and applications of these methods to realistic cases are far from complete.

In a semiclassical approximation the one-dimensional barrier penetration with the Wentzel-Kramers-Brillouin (WKB) approximation is usually used to evaluate the SF half-life. The fission path can be obtained either by minimizing the collective energy in the multidimensional space of coordinates which are used to describe the elongation of the nucleus (e.g., β_{20}), or by minimizing the fission action integral in the collective space. Static fission paths obtained by minimizing the collective energy computed with the macroscopic-microscopic (MM) model [13–15] and various self-consistent mean-field (SCMF) models [16–24] have been used to calculate SF half-lives.

The concept of dynamic least-action fission path was introduced in Refs. [25,26], and subsequently effective methods to determine the dynamic path numerically in a multidimensional collective space were developed [27,28]. Both the potential energy surface and inertia tensors are crucial in determining the dynamic fission path. The ATDHFB method with the perturbative cranking approximation (that is, neglecting the contribution from time-odd mean fields, and treating perturbatively the derivatives of the single-nucleon and pairing densities with respect to collective coordinates) has usually been used in SF fission life-time calculations [25,29–32]. The dynamic fission path, however, can differ significantly from the static one. For instance, it was shown that the triaxial quadrupole degree of freedom plays an important role around the inner and outer barriers along the static fission path for actinide nuclei (Ref. [33] and references therein). Nevertheless, the effect of triaxiality on the dynamic fission

*zhaojie@itp.ac.cn

path is negligible or small in the majority of cases [34–36]. The odd-multipole deformations β_{30} and β_{50} were also found to have a small effect on the dynamic fission path, whereas their inclusion lowers the static fission barrier considerably at large quadrupole deformations [37]. Studies of SF with the least-action principle have also shown that pairing vibrations have a pronounced effect on the fission probability [35,38–45]. Systematic investigations of SF half-lives of superheavy nuclei with the dynamic approach were performed based on the MM [36] and HFB models [18,46].

The nonperturbative cranking ATDHFB collective mass tensor for which the derivatives with respect to collective coordinates are calculated explicitly using numerical techniques was recently used in illustrative calculations of one-dimensional quadrupole fission paths [47]. It was shown that the collective mass exhibits strong variations with the quadrupole collective coordinate, related to changes in the intrinsic shell structure. By using the nonperturbative cranking mass in SF dynamic studies [48] marked triaxial effects were predicted along dynamic fission paths, consistent with those obtained in static calculations, whereas it was found that using the perturbative-cranking mass drives the system towards near-axial shapes. It was noted that the structural properties of the collective mass play an essential role in determining the SF dynamics.

Models based on the framework of relativistic nuclear energy density functionals have been successfully applied to the description of deformation energy landscapes and fission barriers of heavy and superheavy nuclei (Ref. [33] and references therein). By breaking both axial and reflection symmetries, the multidimensionally-constrained relativistic mean-field (MDC-RMF) and multidimensionally-constrained relativistic Hartree Bogoliubov (MDC-RHB) model have recently been developed and implemented in studies of deformation energy maps and fission barriers of actinide nuclei [33,49–54], shapes of hypernuclei [55,56], and nonaxial-octupole Y_{32} correlations in $N = 150$ isotones [57].

In this work we explore the dynamics of SF using the MDC-RHB model. The deformation energy surfaces of ^{264}Fm and ^{250}Fm are computed by solving constrained RHB equations in a multidimensional collective coordinate space. The collective inertia tensor is calculated using the self-consistent RHB solutions and applying the ATDHFB expressions in both the perturbative-cranking and nonperturbative-cranking approximations. The dynamic fission paths are determined by the least-action principle with perturbative-cranking and nonperturbative-cranking inertias, and the corresponding SF half-lives are computed. The article is organized as follows. The theoretical framework is introduced in Sec. II, numerical details of the calculation, the results for the deformation energy landscapes, inertias, and minimum-action fission paths are discussed in Sec. III, and a summary and conclusions are included in Sec. IV.

II. THEORETICAL FRAMEWORK

The tool of choice for theoretical studies of the structure of medium-heavy and heavy nuclei is the framework of energy density functionals (EDFs) [58,59]. Self-consistent mean-field models based on semiempirical EDFs provide an accurate and reliable microscopic description of nuclear structure phenomena over the entire nuclide chart. EDF-based structure models have also been developed that go beyond the static mean-field approximation, and include collective correlations related to the restoration of broken symmetries and to fluctuations of collective variables. Relativistic mean-field (RMF) models present a particular implementation of the nuclear EDF framework. In the standard representation based on the Walecka model, the atomic nucleus is described as a system of Dirac nucleons coupled to exchange mesons through an effective Lagrangian. However, at the energy scale characteristic for nuclear binding low-lying excitations, the meson exchange is just a convenient representation of the effective nuclear interaction, and can be replaced by the local contact interactions between nucleons. To describe nuclear properties at a quantitative level, higher order many-body effects have to be included through a medium dependence of the internucleon interaction. This can be achieved either by including higher-order (nonlinear) terms in the Lagrangian, or by assuming an explicit density dependence for the vertex functions. In the present study we employ two standard and representative point-coupling relativistic EDFs that have been extensively used in studies of a variety of nuclear properties. PC-PK1 [60] includes higher-order interaction terms in the nucleon self-energies, and DD-PC1 [61] with quadratic interaction terms but including explicit density-dependent vertex functions.

For a quantitative description of open-shell nuclei it is necessary to consider also pairing correlations. The relativistic Hartree-Bogoliubov (RHB) framework [59] provides a unified description of particle-hole (ph) and particle-particle (pp) correlations by combining two average potentials: the self-consistent mean field Γ that encloses all the long range ph correlations, and a pairing field Δ which sums up the pp correlations. Here we use a pairing force separable in momentum pace in the pp channel:

$$\langle k|V^{1S_0}|k'\rangle = -Gp(k)p(k'). \tag{1}$$

A simple Gaussian ansatz $p(k) = e^{-a^2k^2}$ in momentum space is assumed and, when transformed from momentum to coordinate space, the interaction takes the form

$$V(\mathbf{r}_1,\mathbf{r}_2,\mathbf{r}_1',\mathbf{r}_2') = G_0\delta(\mathbf{R}-\mathbf{R}')P(\mathbf{r})P(\mathbf{r}')\tfrac{1}{2}(1-P^\sigma), \tag{2}$$

where $\mathbf{R} = (\mathbf{r}_1+\mathbf{r}_2)/2$ and $\mathbf{r} = \mathbf{r}_1-\mathbf{r}_2$ denote the center-of-mass and the relative coordinates, and $P(\mathbf{r})$ is the Fourier transform of $p(k)$,

$$P(\mathbf{r}) = \frac{1}{(4\pi a^2)^{3/2}}e^{-\mathbf{r}^2/4a^2}. \tag{3}$$

The two parameters G_0 and a have been adjusted to reproduce the density dependence of the pairing gap in nuclear matter at the Fermi surface. The pairing gap calculated with the D1S parametrization of the Gogny force [5] is reproduced using the interaction (2) with the following values: $G_0 = -738$ MeV fm^{-3} and $a = 0.644$ fm [62].

The deformation energy landscape is obtained in a self-consistent mean-field calculation with constraints on mass

multipole moments [7]. Here we use a modified linear-constraint method with the Routhian defined as

$$E' = E_{RHB} + \sum_{\lambda\mu} \frac{1}{2} C_{\lambda\mu} Q_{\lambda\mu}. \tag{4}$$

In each iteration step the coefficients $C_{\lambda\mu}$ are modified:

$$C_{\lambda\mu}^{(n+1)} = C_{\lambda\mu}^{(n)} + k_{\lambda\mu}\left(\beta_{\lambda\mu}^{(n)} - \beta_{\lambda\mu}\right), \tag{5}$$

where $\beta_{\lambda\mu}$ is the desired deformation, $k_{\lambda\mu}$ is a constant, and $C_{\lambda\mu}^{(n)}$ denotes the value of the coefficient in the nth iteration step.

To describe nuclei with general quadrupole and/or octupole shapes, the Dirac-Hartree-Bogoliubov equations are solved by expanding the nucleon spinors in the basis of a three-dimensional (3D) harmonic oscillator in Cartesian coordinates. Basis states satisfying $[n_z/Q_z + (2n_\rho + |m_l|)/Q_\rho] \leqslant N_f$ are included for the large component of the Dirac single-nucleon wave function, where $Q_z = \max(1, b_z/b_0)$ and $Q_\rho = \max(1, b_\rho/b_0)$ are constants related to the oscillator lengths $b_0 = 1/\sqrt{M\omega_0}$, b_z, and b_ρ. For the small component of the Dirac spinor $N_g = N_f + 1$ major shells are included in order to avoid the occurrence of spurious states [63]. In the present study of transactinide nuclei calculations have been performed in a basis with $N_f^{\max} = 16$ shells.

The nuclear shape is parametrized by the deformation parameters

$$\beta_{\lambda\mu} = \frac{4\pi}{3AR^\lambda}\langle Q_{\lambda\mu}\rangle, \tag{6}$$

where $Q_{\lambda\mu} = r^\lambda Y_{\lambda\mu}$ is the mass multipole operator. The shape is assumed to be invariant under the exchange of the x and y axes and all deformations $\beta_{\lambda\mu}$ with even μ can be included simultaneously. For details of the MDC-RMF model we refer the reader to Ref. [33].

We will explore the spontaneous fission (SF) process along a fission path L that is embedded in the multidimensional collective space. The path is defined by the parameter s with the inner (s_{in}) and outer (s_{out}) turning points. The fission action integral reads

$$S(L) = \int_{s_{\text{in}}}^{s_{\text{out}}} \frac{1}{\hbar}\sqrt{2\mathcal{M}_{\text{eff}}(s)[V_{\text{eff}}(s) - E_0]}ds, \tag{7}$$

where $\mathcal{M}_{\text{eff}}(s)$ and $V_{\text{eff}}(s)$ are the effective collective inertia and potential along the fission path $L(s)$, respectively. E_0 is the collective ground state energy, and the integration limits correspond to the classical inner and outer turning points defined by $V_{\text{eff}}(s) = E_0$. The fission path $L(s)$ is determined by minimizing the action integral in Eq. (7) [25,26]. The SF half-life is calculated as $T_{1/2} = \ln 2/(nP)$, where n is the number of assaults on the fission barrier per unit time [27,28,42,48], and P is the barrier penetration probability in the WKB approximation

$$P = \frac{1}{1 + \exp[2S(L)]}. \tag{8}$$

The essential ingredients in the calculation of the action integral, expression (7), are the effective collective inertia and potential. The effective inertia is related to the multidimensional collective inertia tensor $\mathcal{M}$ [25,27,28,42,48]:

$$\mathcal{M}_{\text{eff}}(s) = \sum_{ij} \mathcal{M}_{ij} \frac{dq_i}{ds}\frac{dq_j}{ds}\ , \tag{9}$$

where $q_i(s)$ denotes the collective variable as function of the path's length.

The collective inertia tensor is computed using the ATD-HFB method [47]. In the nonperturbative cranking approximation the inertia tensor reads

$$\mathcal{M}_{ij}^C = \frac{\hbar^2}{2\dot{q}_i\dot{q}_j} \sum_{\alpha\beta} \frac{F_{\alpha\beta}^{i*}F_{\alpha\beta}^{j} + F_{\alpha\beta}^{i}F_{\alpha\beta}^{j*}}{E_\alpha + E_\beta}, \tag{10}$$

where

$$\frac{F^i}{\dot{q}_i} = U^\dagger \frac{\partial \rho}{\partial q_i} V^* + U^\dagger \frac{\partial \kappa}{\partial q_i} U^* - V^\dagger \frac{\partial \rho^*}{\partial q_i} U^* - V^\dagger \frac{\partial \kappa^*}{\partial q_i} V^*\ . \tag{11}$$

U and V are the self-consistent Bogoliubov matrices, and ρ and κ are the corresponding particle and pairing density matrices, respectively. The derivatives of the densities are calculated using the Lagrange three-point formula for unequally spaced points [64,65]. The formula Eq. (11) can be further simplified by using a perturbative approach [25,29–32], with the resulting perturbative cranking inertia

$$\mathcal{M}^{Cp} = \hbar^2 M_{(1)}^{-1} M_{(3)} M_{(1)}^{-1}, \tag{12}$$

and with

$$[M_{(k)}]_{ij} = \sum_{\alpha\beta} \frac{\langle 0|\hat{Q}_i|\alpha\beta\rangle\langle\alpha\beta|\hat{Q}_j|0\rangle}{(E_\alpha + E_\beta)^k}. \tag{13}$$

$|\alpha\beta\rangle$ are two-quasiparticle wave functions. Details of the derivation of the formulas for the inertia tensor can be found in Ref. [47].

The effective collective potential V_{eff} is obtained by subtracting the vibrational zero-point energy (ZPE) from the total RHB deformation energy. Following the prescription of Refs. [18,42,48,66] the ZPE is computed using the Gaussian overlap approximation,

$$E_{\text{ZPE}} = \tfrac{1}{4}\text{Tr}\left[M_{(2)}^{-1}M_{(1)}\right], \tag{14}$$

where the $M_{(k)}$ are given by Eq. (13). The microscopic self-consistent solutions of the constrained RHB equations, that is, the single-quasiparticle energies and wave functions on the entire energy surface as functions of the quadrupole deformations, provide the microscopic input for the calculation of the collective inertia and zero-point energy.

III. SPONTANEOUS FISSION OF ^{264}Fm AND ^{250}Fm

We analyze two illustrative examples: the symmetric spontaneous fission of ^{264}Fm and the asymmetric SF of ^{250}Fm. Although in principle one could include arbitrary many collective coordinates in the description of the fission process, in practice available computational resources impose rather severe restrictions on the dimensionality of the collective space in self-consistent calculations. The present study is restricted to

a two-dimensional collective space defined by either (β_{20},β_{22}) (quadrupole triaxial) or (β_{20},β_{30}) (quadrupole and octupole axial) collective coordinates.

Two relativistic NEDFs, PC-PK1 with nonlinear self-interaction terms [60], and DD-PC1 functional with density-dependent couplings [61], are used in the self-consistent RHB calculations of the deformation energy surfaces, collective inertia tensors, and fission action integrals. We note that the height of the fission barriers is rather sensitive to the strength of the pairing interaction [67]. Thus, the particular choice of the pairing strength may considerably affect the fission dynamics. As explained above, the parameters of the finite range separable pairing force were originally adjusted to reproduce the pairing gap at the Fermi surface in symmetric nuclear matter as calculated with the Gogny D1S force. However, a number of studies based on the relativistic Hartree-Bogoliubov model have shown that the pairing strength needs to be fine-tuned in some cases, especially for heavy nuclei [68,69]. In this study the pairing strengths are further adjusted to reproduce the available empirical pairing gaps in Fm isotopes. The resulting values with respect to the original pairing strength adjusted in nuclear matter ($G_0 = -738$ MeV fm^{-3})are $G_n/G_0 = 1.06$, $G_p/G_0 = 1.04$ for PC-PK1, and $G_n/G_0 = 1.11$, $G_p/G_0 = 1.08$ for DD-PC1. As in Refs. [42,48], we choose $E_0 = 1$ MeV in Eq. (7) for the value of the collective ground state energy. Although arbitrary, this choice enables a direct comparison of our results with those reported in previous studies. For the vibrational frequency $\hbar\omega_0 = 1$ MeV the number of assaults on the fission barrier per unit is $10^{20.38}$ s^{-1} [46].

A. Symmetric fission of ^{264}Fm

Previous theoretical studies of ^{264}Fm [19,70] have shown that one can expect this nucleus to undergo symmetric spontaneous fission and, therefore, we do not consider reflection-asymmetric degrees of freedom and perform the analysis in the collective space (β_{20},β_{22}). Figure 1 displays the self-consistent triaxial quadrupole deformation energy surfaces of ^{264}Fm in the (β_{20},β_{22}) plane. The energy surfaces in the upper (lower) panel are calculated with the density functionals PC-PK1 (DD-PC1), and the pairing interaction Eq. (2) The functional PC-PK1 predicts an axially symmetric equilibrium (ground) state with moderate elongation ($\beta_{20} \approx 0.2$). The axially symmetric barrier at $\beta_{20} \approx 0.6$ is bypassed through the triaxial region, thus lowering the height of the barrier by $\approx$2 MeV. With DD-PC1 a similar energy surface is obtained, however, with a more pronounced influence of the triaxial degree of freedom on the height of the barrier.

The collective potential is obtained by subtracting the vibrational ZPE ($E_{\rm ZPE}$) from the total binding energy surface. In Fig. 2 we plot the vibrational ZPE Eq. (14), normalized with respect to the mean-field ground state. The two functionals lead to rather similar results, and the deformation dependence of the ZPEs is comparable to the results obtained in Ref. [48] using the Skyrme energy density functional SkM* and a density dependent mixed pairing interaction.

To calculate the fission action integral one has to compute the collective inertia tensor $\mathcal{M}_{ij}$. Although perturbative cranking mass parameters have been used in numerous studies, the

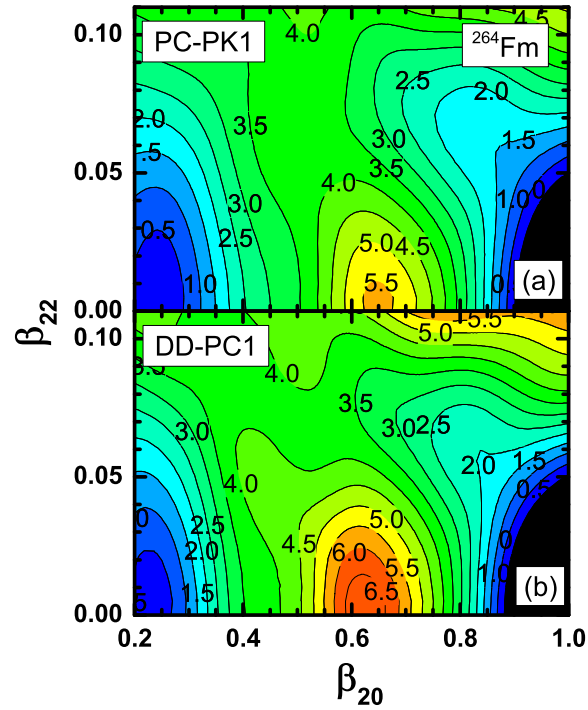

FIG. 1. (Color online) RHB self-consistent triaxial quadrupole constrained energy surfaces of ^{264}Fm in the (β_{20},β_{22}) plane. In each panel energies are normalized with respect to the binding energy of the equilibrium minimum, and contours join points on the surface with the same energy (in MeV). The energy surfaces in (a) [(b)] are calculated with the density functionals PC-PK1 [60] (DD-PC1 [61]), and the pairing interaction Eq. (2).

importance of the exact treatment of derivatives of single-particle and pairing densities in the ATDHFB expressions for the mass parameters has recently been emphasized [48]. For the two-dimensional space of collective deformation coordinates three independent components $\mathcal{M}_{11}$, $\mathcal{M}_{12}$, and $\mathcal{M}_{22}$ determine the inertia tensor and, in this case, the indices 1 and 2 refer to the β_{20} and β_{22} degrees of freedom, respectively. The difference between the perturbative and nonperturbative cranking approximations is clearly seen in the top panel of Fig. 3, where we plot the $\mathcal{M}_{11}$ component of the collective inertia tensor as a function of β_{20} for axial symmetry ($\beta_{22} = 0$). The solid (red) curve denotes the nonperturbative cranking mass parameter, whereas the dot-dashed (black) curve corresponds to the perturbative cranking mass parameter. $\mathcal{M}_{11}^{Cp}$ displays a smooth dependence on the deformation parameter β_{20} and, although one notices some fluctuations, their magnitude is small. The deformation dependence of the nonperturbative cranking mass parameter $\mathcal{M}_{11}^{C}$ follows the perturbative result $\mathcal{M}_{11}^{Cp}$, however, several sharp peaks occur at deformations $\beta_{20} \approx 0.4$, $\beta_{20} \approx 0.6$, and $\beta_{20} \approx 0.8$. To understand better these results, in Fig. 3 we also plot the binding energy (middle panel) and the self-consistent value of the β_{40} deformation parameter (bottom panel). We notice that the most pronounced peak, located at $\beta_{20} \approx 0.6$, actually corresponds to the position of the fission barrier. In general, the occurrence of sharp peaks in the collective mass is related to single-particle level

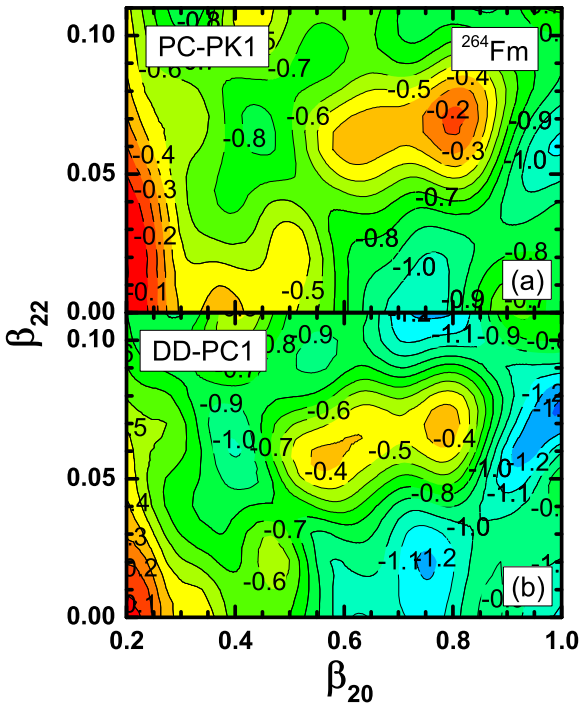

FIG. 2. (Color online) The vibrational zero-point energies $E_{\rm ZPE}$ Eq. (14) of ^{264}Fm in the (β_{20},β_{22}) plane. Energy surfaces obtained with the PC-PK1 and DD-PC1 functionals are compared in (a) and (b), respectively. In each panel energies are normalized with respect to the the equilibrium minimum, and contours join points on the surface with the same energy (in MeV).

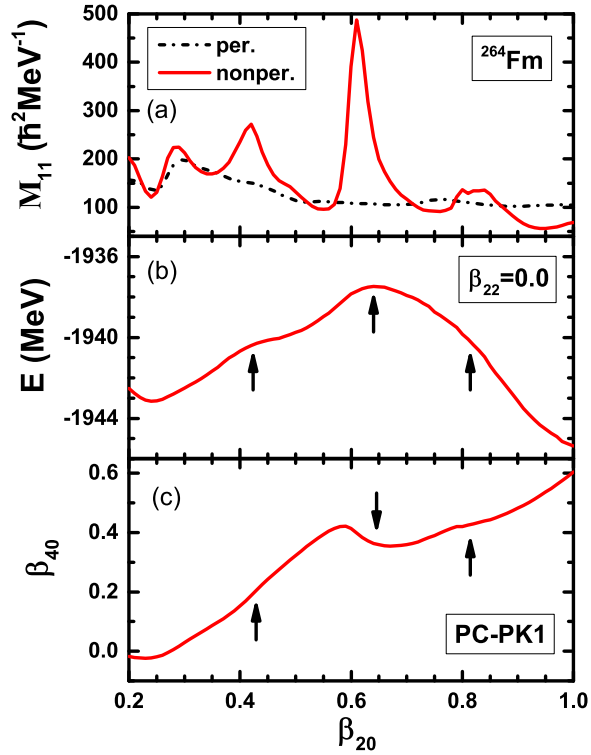

FIG. 3. (Color online) The $\mathcal{M}_{11}$ component of the inertia tensor (a), the binding energy (b), and the self-consistent deformation parameter β_{40} (c) of ^{264}Fm as functions of the deformation β_{20}. Axial symmetry $\beta_{22} = 0$ is imposed, and the functional PC-PK1 is used in the RHB calculation.

crossings near the Fermi surface, that is, to abrupt changes of occupied single-particle configurations in a specific nucleus [47,48]. Such pronounced structural rearrangements lead to strong variations in the derivatives of densities in Eq. (11), and consequently sharp peaks develop in the nonperturbative cranking collective inertia. At these specific deformations the value of the nonperturbative collective inertia can be several times larger than the corresponding perturbative inertia, and this shows that the effects of level crossing are not properly taken into account in the perturbative cranking approach.

The collective inertia tensors can be visualized by plotting the square-root determinant

$$|\mathcal{M}|^{1/2} = \left(\mathcal{M}_{11}\mathcal{M}_{22} - \mathcal{M}_{12}^2\right)^{1/2}, \tag{15}$$

invariant with respect to rotations in the two-dimensional collective space [48]. In Figs. 4 and 5 we compare results obtained in a triaxial calculation with the perturbative and nonperturbative approaches, and using the functionals PC-PK1 and the DD-PC1. Although both approaches lead to rather complex topographies of $|\mathcal{M}|^{1/2}$ in the (β_{20},β_{22}) plane, we note more pronounced variations for the nonperturbative approach. In particular, the nonperturbative calculation results in very large values of $|\mathcal{M}|^{1/2}$ in the region of the axial fission barrier, consistent with the behaviour of the component $\mathcal{M}_{11}$ for the axial case (cf. Fig. 3).

The minimum action path is determined using two different numerical minimization techniques: the dynamic-programming method (DPM) [28], and the Ritz method (RM) [27]. The DPM is implemented by discretizing the energy surface in the (β_{20},β_{22}) plane with an equidistant two-dimensional mesh. After considering all possible combinations of mesh points, the fission path is constructed by connecting those points that minimize the action integral. The RM, on the other hand, is implemented by expressing the trial path as a Fourier series of collective coordinates. The coefficients of this series are determined by minimizing the action integral. We note that for both methods we have considered several possible values for the turning points $s_{\rm in}$ and $s_{\rm out}$ to make certain that the minimum action path is chosen. Details about the implementation of both the DPM and the RM are included in the Appendix.

The spontaneous fission paths on the triaxial deformation energy surface of ^{264}Fm are shown in Fig. 6. Four different paths are included in the figure: DPM+$\mathcal{M}^{Cp}$ path (dotted line), RM+$\mathcal{M}^{Cp}$ (dash-dot-dot), DPM+$\mathcal{M}^{C}$ path (dash-dotted), and RM+$\mathcal{M}^{C}$ (solid). The static path, determined by following the points of minimum energy between the turning points, is also shown for comparison (long dashed). It is interesting to note that, although they correspond to completely different effective interactions and were adjusted to data following different procedures, both PC-PK1 and DD-PC1 predict very similar paths. Similar SF paths are also obtained using the perturbative and nonperturbative cranking inertia parameters. The paths detour the axial barrier through

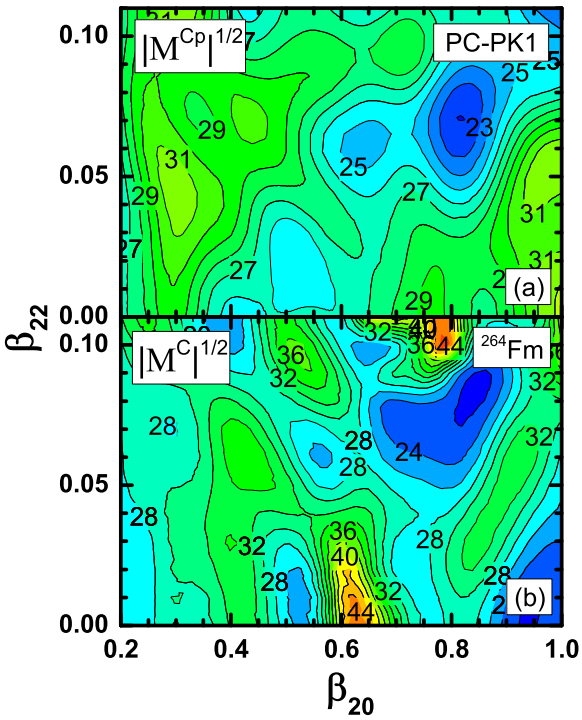

FIG. 4. (Color online) Square-root determinants of the perturbative-cranking inertia tensor $|\mathcal{M}^{Cp}|^{1/2}$ (a), and nonperturbative-cranking inertia tensor $|\mathcal{M}^{C}|^{1/2}$ (b) (in $10 \times \hbar^2\,\mathrm{MeV}^{-1}$), of ^{264}Fm in the (β_{20},β_{22}) plane. The functional PC-PK1 is used in the RHB calculation.

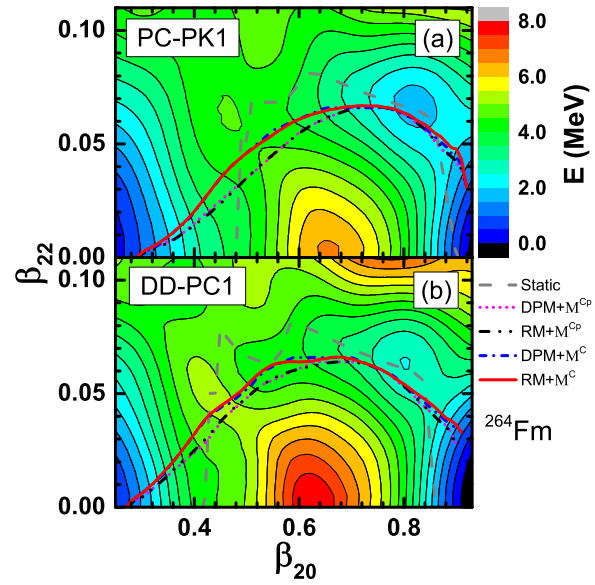

FIG. 6. (Color online) Dynamic paths for spontaneous fission of ^{264}Fm in the (β_{20},β_{22}) plane, calculated with the functionals PC-PK1 (a) and DD-PC1 (b). The nonperturbative and perturbative cranking inertia are used, together with the DMP and RM techniques for the minimization of the collective action. The dotted and dash-dot-dot curves denote paths calculated with the perturbative-cranking inertia tensors using the DMP and RM, respectively, while the corresponding paths obtained with the nonperturbative-cranking inertia are plotted with the dash-dotted (solid) curves. The static path (dashed curve) is also shown for comparison.

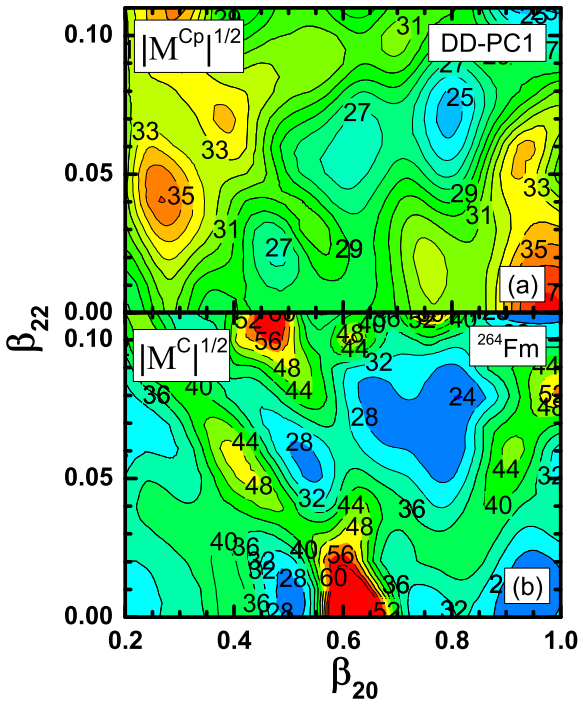

FIG. 5. (Color online) Same as described in the caption to Fig. 4 but for the functional DD-PC1.

the triaxial region, although the excursion to the triaxial region is more pronounced for the nonperturbative cranking inertia. The present result differs somewhat from those obtained using the macroscopic-microscopic approach [34–36], and the nonrelativistic HFB model [16,48], where for the perturbative cranking inertia the nucleus ^{264}Fm chooses an almost axially symmetric path towards fission. The resulting values of the action integral and the fission half-lives are summarized in Table I. Although very similar paths are obtained with PC-PK1 and DD-PC1, the corresponding values of the action integral differ by more than 20%, which leads to orders of magnitude difference in the calculated fission half-lives. The difference between the perturbative and nonperturbative ATDHFB approximations for the collective inertia parameter is consistent for both functionals. We also note that both minimization techniques produce virtually identical results for the action integral, and this provides a reliable test for the numerical accuracy and stability of the present calculation. Finally, it appears that the results obtained with the functional DD-PC1 are somewhat closer to those of Ref. [48], calculated with the Skyrme functional SkM*, and very similar in the dynamical calculation with the nonperturbative cranking collective inertia. We find that the triaxial degree of freedom always plays an important role in SF dynamics, independent of the approximation used to compute the inertia tensor. However, the calculated half-lives are sensitive to the collective inertia. The nonperturbative cranking mass predicts larger

TABLE I. Values for the action integral and SF half-lives of ^{264}Fm that correspond to the paths displayed in Fig. 6. The results obtained in the present analysis (PC-PK1 and DD-PC1) are compared with those from Ref. [48].

EDF	Path	$S(L)$	$\log_{10}(T_{1/2}/\mathrm{yr})$
PC-PK1	Static+$\mathcal{M}^{Cp}$	18.52	−11.96
	Static+$\mathcal{M}^{C}$	19.69	−10.94
	DPM+$\mathcal{M}^{Cp}$	14.52	−15.43
	RM+$\mathcal{M}^{Cp}$	14.49	−15.45
	DPM+$\mathcal{M}^{C}$	15.53	−14.55
	RM+$\mathcal{M}^{C}$	15.48	−14.59
DD-PC1	Static+$\mathcal{M}^{Cp}$	23.71	−7.44
	Static+$\mathcal{M}^{C}$	27.07	−4.53
	DPM+$\mathcal{M}^{Cp}$	17.84	−12.54
	RM+$\mathcal{M}^{Cp}$	17.81	−12.57
	DPM+$\mathcal{M}^{C}$	19.74	−10.89
	RM+$\mathcal{M}^{C}$	19.71	−10.91
SkM* [48]	Static+$\mathcal{M}^{Cp}$	20.8	−10.0
	Static+$\mathcal{M}^{C}$	23.4	−7.7
	DPM+$\mathcal{M}^{Cp}$	16.8	−13.4
	RM+$\mathcal{M}^{Cp}$	16.8	−13.4
	DPM+$\mathcal{M}^{C}$	19.1	−11.4
	RM+$\mathcal{M}^{C}$	18.9	−11.6

values of the fission action integral $S(L)$ and, therefore, longer half-lives.

B. Asymmetric fission of ^{250}Fm

In the next example we explore the influence of the reflection-asymmetric degree of freedom on the spontaneous fission process and study the asymmetric spontaneous fission ^{250}Fm [70]. Since the complete calculation in the three-dimensional collective space (β_{20}, β_{22}, and β_{30}) is computationally too demanding, we simplify the problem by determining the spontaneous fission dynamic path in two intervals: i) the path that connects the mean-field ground state and the isomeric state is calculated in the (β_{20},β_{22}) plane, and ii) the path between the isomeric state and the outer turning point is determined in the (β_{20},β_{30}) plane. The optimal path is obtained by combining the paths in the (β_{20},β_{22}) and (β_{20},β_{30}) plane with the isomeric state as the matching point.

In Fig. 7(a) we display the RHB (DD-PC1 plus separable pairing) deformation energy energy surface of ^{250}Fm in the (β_{20},β_{30}) plane. The mean-field equilibrium (ground) state is predicted at moderate quadrupole deformation $\beta_{20} \approx 0.3$, and the isomeric minimum at $\beta_{20} \approx 0.95$. We note that through the entire region of quadrupole deformations $\beta_{20} \leqslant 1.4$, the nucleus remains reflection symmetric, that is, octupole degrees of freedom need not be included for this range of quadrupole deformations. The region around the inner fission barrier is further analyzed in Fig. 7(b), where we plot the energy surface of ^{250}Fm in the (β_{20},β_{22}) plane. Note the different horizontal scales in the two panels. The inclusion of the triaxial degree of freedom lowers the barrier by ≈2 MeV, and this effect is similar in magnitude to the case of ^{264}Fm analyzed in the previous section. Since triaxial shapes have

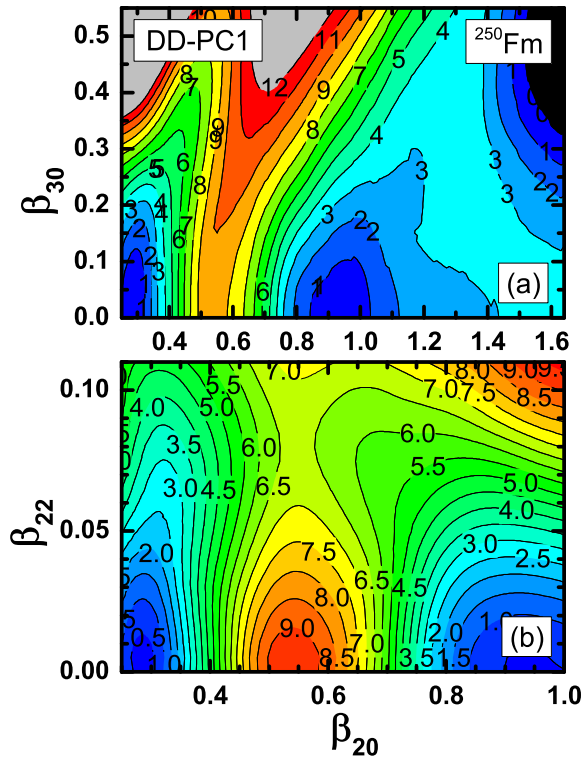

FIG. 7. (Color online) RHB (DD-PC1 plus separable pairing) self-consistent constrained energy surfaces of ^{250}Fm in the (β_{20},β_{30}) (a) and (β_{20},β_{22}) (b) planes. In each panel energies are normalized with respect to the binding energy of the equilibrium minimum, and contours join points on the surface with the same energy (in MeV).

the largest effect in the region of the first fission barrier, and reflection-asymmetric degrees of freedom are important for large quadrupole deformations, dividing the fission path into two segments provides a reasonable approximation for the complex multidimensional fission process. The vibrational zero-point energies of ^{250}Fm isotope in the (β_{20},β_{22}) plane (b) and the (β_{20},β_{30}) plane (a) are shown in Fig. 8. For the whole deformation range considered in this figure the variation of E_{ZPE} is approximately 2 MeV, and very similar results are obtained with the functional PC-PK1. Note, however, the difference of the ZPE in the lower panel with respect to the quadrupole zero-point energy of ^{264}Fm shown in Fig. 2.

The deformation dependence of the collective inertia tensor is illustrated in Figs. 9 and 10, where we plot the square-root determinant $|\mathcal{M}|^{1/2} = (\mathcal{M}_{11}\mathcal{M}_{22} - \mathcal{M}_{12}^2)^{1/2}$ in the (β_{20},β_{30}) and (β_{20},β_{22}) planes, respectively. The perturbative cranking inertias $|\mathcal{M}^{Cp}|^{1/2}$ are shown in the upper panels, and the lower panels display the square-root determinants $|\mathcal{M}^{C}|^{1/2}$ of the nonperturbative cranking inertia tensor. The calculation of Fig. 9 corresponds to axially symmetric but reflection asymmetric shapes, that is, the indices 1 and 2 denote the β_{20} and β_{30} collective degrees of freedom, respectively. Figure 10 shows the deformation dependence of the square-root determinants of collective inertia when the shape is allowed to be triaxial but reflection symmetry is assumed. In this case the indices 1 and 2 denote the coordinates β_{20} and β_{22}, respectively. The overall

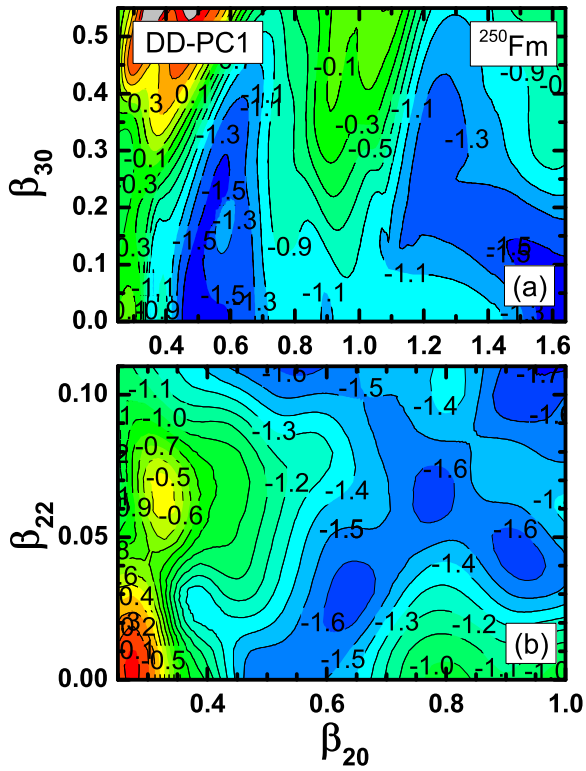

FIG. 8. (Color online) The vibrational zero-point energies $E_{\rm ZPE}$ Eq. (14) of ^{250}Fm in the (β_{20},β_{30}) plane (a), and the (β_{20},β_{22}) plane (b). Energies are normalized with respect to the the equilibrium minimum, and contours join points with the same energy (in MeV). The functional DD-PC1 is used in the RHB calculation.

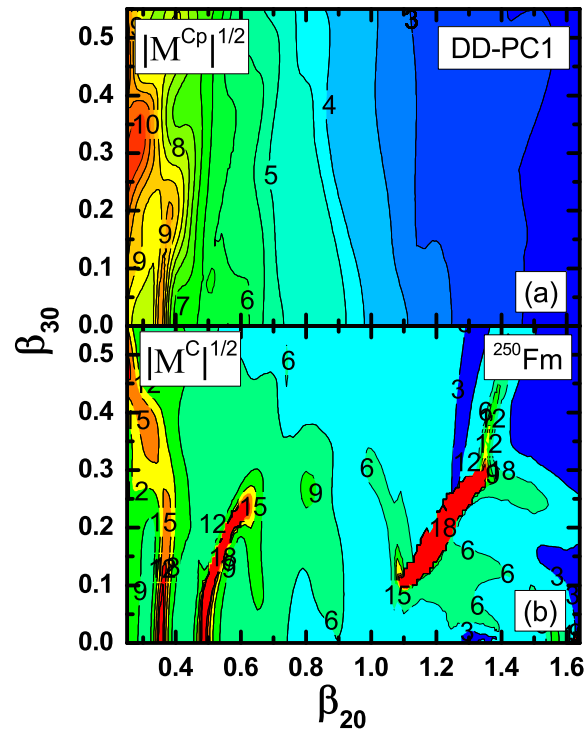

FIG. 9. (Color online) Square-root determinants of the perturbative cranking inertia tensor $|\mathcal{M}^{Cp}|^{1/2}$ (a), and nonperturbative cranking inertia tensor $|\mathcal{M}^{C}|^{1/2}$ (b) (in $10\times\hbar^2\,\mathrm{MeV}^{-1}$), of ^{250}Fm in the (β_{20},β_{30}) plane. The calculation corresponds to axially symmetric but reflection asymmetric shapes.

deformation dependence of $|\mathcal{M}^{Cp}|^{1/2}$ and $|\mathcal{M}^{C}|^{1/2}$ in Fig. 9 is similar but the nonperturbative cranking mass parameter displays several sharp peaks due to the crossing of single-particle levels around the Fermi surface (see the discussion in the previous section). The picture is markedly different in the triaxial but reflection symmetric case illustrated in Fig. 10, where the square-root determinant of the perturbative cranking collective inertia exhibits a smooth dependence in both β_{20} and β_{22} directions, whereas the nonperturbative cranking inertia displays rapid fluctuations with very pronounced peak values caused by the level crossing effect. Similar results are also obtained with the functional PC-PK1, not shown here.

In the case of ^{250}Fm both the quadrupole triaxial β_{22} and octupole β_{30} collective degrees of freedom play an important role in the spontaneous fission process. However, the calculation of the dynamic fission path in the full 3D collective space (β_{20}, β_{22}, and β_{30}), because of the huge number of computations required, is presently beyond our computational capabilities. For this reason, in the first step we determine the path in the restricted 2D collective space (β_{20},β_{30}). The results are shown in Fig. 11, where we compare the fission paths calculated using the functionals PC-PK1 (upper panel), and DD-PC1 (lower panel). For both cases the perturbative approach to calculating the collective inertia produces a path which is close to the static one (minimum energy path). The dynamic path determined within the nonperturbative cranking

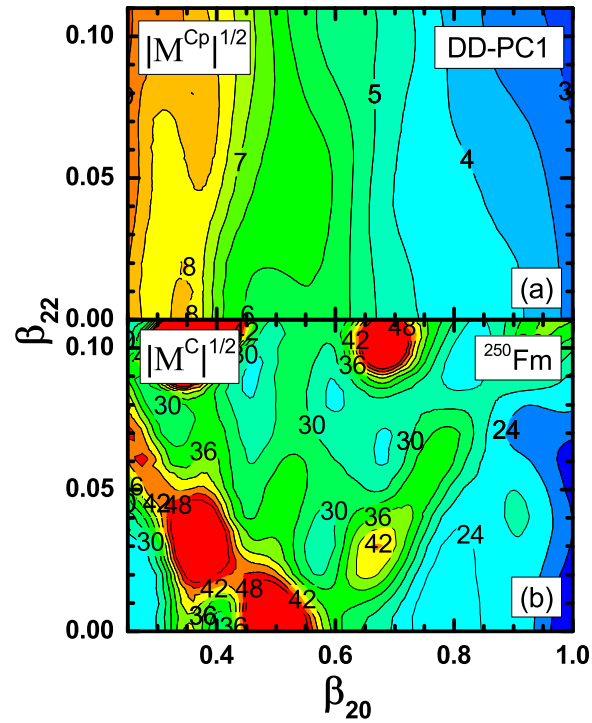

FIG. 10. (Color online) Same as described in the caption to Fig. 9 but for the inertia tensor in the (β_{20},β_{22}) plane. In this case the shape is allowed to be triaxial but reflection symmetry is assumed.

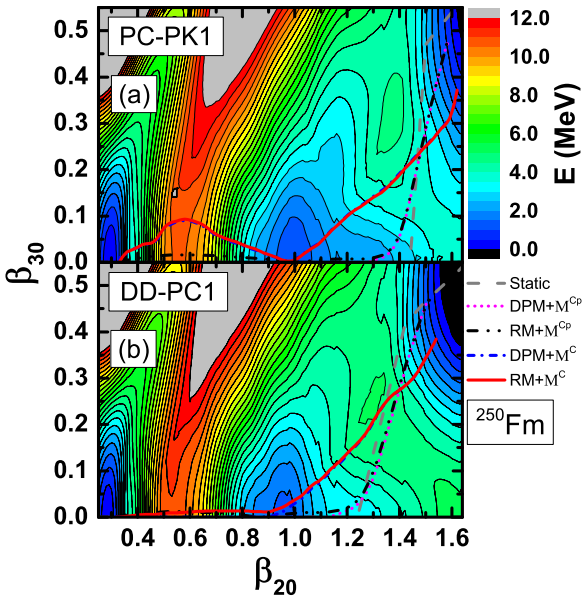

FIG. 11. (Color online) Dynamic paths for spontaneous fission of ^{250}Fm in the (β_{20},β_{30}) collective space with the perturbative and non-perturbative cranking inertia tensors. Both the dynamic-programming method and the Ritz method have been used to minimize the fission action integral. The static path (dashed curve) is also plotted for comparison. The results are obtained with the functionals PC-PK1 (a) and DD-PC1 (b), and axial symmetry is assumed.

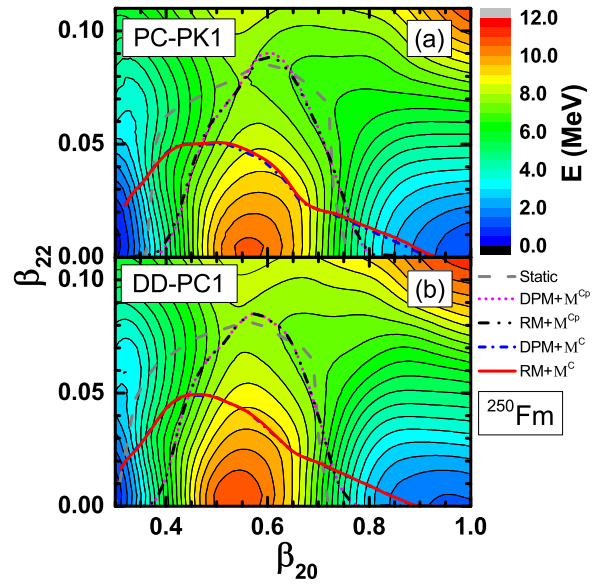

FIG. 12. (Color online) Same as described in the caption to Fig. 11 but for the paths in the (β_{20},β_{22}) plane. The shape is allowed to be triaxial but reflection symmetric.

inertia is markedly different and, for PC-PK1, it even makes an excursion in the reflection-asymmetric region already in the vicinity of the inner barrier. The corresponding action integrals and fission half-lives are listed in Table II. We note that in both cases the path passes through the isomeric state ($\beta_{20} \approx 0.95$, $\beta_{30} = 0$, $\beta_{22} = 0$) which, in fact, is the common point for the two deformation spaces (β_{20},β_{30}) and (β_{20},β_{22}). Hence, the isomeric state presents the most reasonable choice for the matching point at which the two paths are combined.

As shown in the lower panel of Fig. 7 the effects of triaxiality cannot be neglected in the region around the inner fission barrier. To take this degree of freedom into account we calculate the fission path in the (β_{20},β_{22}) collective space, connecting the mean-field ground state and the isomeric state. The results are displayed in Fig. 12. Also in this case using the perturbative cranking collective inertia produces a path similar to the static one, whereas including the nonperturbative cranking inertia modifies the path considerably. Although in the nonperturbative approach the paths do not reach that far in the triaxial region as the static and perturbative cranking dynamic paths, triaxial effects are obviously important for a realistic description of the spontaneous fission process of this isotope. In Table III we list the values of the action integral

TABLE II. Values for the action integral and SF half-lives of ^{250}Fm that correspond to the paths displayed in Fig. 11. The results obtained with the functionals PC-PK1 and DD-PC1 correspond to the axially symmetric calculation in the (β_{20},β_{30}) plane.

EDF	Path	$S(L)$	$\log_{10}(T_{1/2}/\mathrm{yr})$
PC-PK1	DPM+$\mathcal{M}^{Cp}$	28.23	−3.52
	RM+$\mathcal{M}^{Cp}$	28.23	−3.52
	DPM+$\mathcal{M}^{C}$	33.01	0.64
	RM+$\mathcal{M}^{C}$	32.97	0.60
DD-PC1	DPM+$\mathcal{M}^{Cp}$	30.74	−1.34
	RM+$\mathcal{M}^{Cp}$	30.73	−1.35
	DPM+$\mathcal{M}^{C}$	35.67	2.95
	RM+$\mathcal{M}^{C}$	35.60	2.89

TABLE III. Values of the action integral for different fission paths of ^{250}Fm, connecting the inner turning point and the isomeric state. The label AXIAL denotes paths determined in the (β_{20},β_{30}) collective space, while the paths denoted with TRIAXIAL correspond to the collective space (β_{20},β_{22}).

EDF	Symmetry	Path	$S(L)$
PC-PK1	AXIAL	DPM+$\mathcal{M}^{Cp}$	20.61
		RM+$\mathcal{M}^{Cp}$	20.60
		DPM+$\mathcal{M}^{C}$	24.80
		RM+$\mathcal{M}^{C}$	24.46
	TRIAXIAL	DPM+$\mathcal{M}^{Cp}$	19.57
		RM+$\mathcal{M}^{Cp}$	19.57
		DPM+$\mathcal{M}^{C}$	23.60
		RM+$\mathcal{M}^{C}$	23.54
DD-PC1	AXIAL	DPM+$\mathcal{M}^{Cp}$	21.43
		RM+$\mathcal{M}^{Cp}$	21.42
		DPM+$\mathcal{M}^{C}$	25.65
		RM+$\mathcal{M}^{C}$	25.60
	TRIAXIAL	DPM+$\mathcal{M}^{Cp}$	20.36
		RM+$\mathcal{M}^{Cp}$	20.35
		DPM+$\mathcal{M}^{C}$	24.50
		RM+$\mathcal{M}^{C}$	24.44

TABLE IV. Values for the action integral and SF half-lives of ^{250}Fm that correspond to the triaxial and reflection-symmetric paths from the inner turning point to the isomeric minimum (cf. Fig. 12), and axial and reflection-asymmetric from the isomer to the outer turning point(cf. Fig. 11).

EDF	Path	$S(L)$	$\log_{10}(T_{1/2}/\mathrm{yr})$
PC-PK1	DPM+$\mathcal{M}^{Cp}$	27.19	−4.42
	RM+$\mathcal{M}^{Cp}$	27.20	−4.41
	DPM+$\mathcal{M}^{C}$	31.81	−0.41
	RM+$\mathcal{M}^{C}$	32.05	−0.20
DD-PC1	DPM+$\mathcal{M}^{Cp}$	29.67	−2.27
	RM+$\mathcal{M}^{Cp}$	29.66	−2.28
	DPM+$\mathcal{M}^{C}$	34.52	1.95
	RM+$\mathcal{M}^{C}$	34.44	1.88

calculated along the paths connecting the mean-field ground state and the isomeric state. The paths labeled with AXIAL and TRIAXIAL are determined in the (β_{20},β_{30}) (cf. Fig. 11) and (β_{20},β_{22}) (cf. Fig. 12) collective space, respectively. One notices that, for both functionals, the inclusion of the triaxial degree of freedom reduces the value of the action integral. For larger quadrupole β_{20} deformations triaxial effects are less important, whereas the octupole degree of freedom plays a critical role in this region, as shown in Fig. 11.

Finally we combine the two segments: triaxial and reflection-symmetric from the inner turning point to the isomeric minimum at $\beta_{20} \approx 0.95$, and axial and reflection-asymmetric from the isomer to the outer turning point, to construct the entire dynamic fission path of ^{250}Fm. The resulting action integrals and fission lifetimes are listed in Table IV. For both functionals the action integrals calculated with the nonperturbative cranking collective inertia are considerably larger (≈5 units) than those obtained with the perturbative cranking inertia. Consequently, the nonperturbative calculation predicts half-lives that are ≈4 orders of magnitude longer in comparison to the perturbative approach. One also notices that the functional DD-PC1 predicts larger action integrals and longer fission half-lives when compared to PC-PK1, both for the perturbative and nonperturbative cranking inertia. This is consistent with the results obtained in the previous section for the symmetric fission of ^{264}Fm. The effect of triaxiality on the asymmetric fission of ^{250}Fm can be estimated by comparing the action integrals and fission life-times listed in Table II (axial and reflection-asymmetric from the inner to the outer turning points) and Table IV (triaxial and reflection symmetric up to the isomeric state, axial and reflection-asymmetric from the isomer to the outer turning point). We note that the inclusion of the triaxial degree of freedom lowers the value of the action integral and shortens the SF half-life of ^{250}Fm, for both functionals and both approximations to the collective inertia.

IV. SUMMARY AND OUTLOOK

We have explored the dynamics of spontaneous fission of the nuclei ^{264}Fm and ^{250}Fm in a theoretical framework based on relativistic energy density functionals. Deformation energy surfaces, collective potentials, and perturbative and nonperturbative ATDHFB cranking collective inertia tensors have been calculated with the multidimensionally-constrained relativistic Hartree-Bogoliubov (MDC-RHB) model, using the energy density functionals PC-PK1 and DD-PC1, and pairing correlations taken into account by a separable pairing force of finite range. Both the static (minimum energy) and dynamic (least action) fission paths, as well as the corresponding SF half-lives have been analyzed. For both nuclei considered in this study triaxial deformations lower the inner barrier by about 3 MeV along the static fission path. The ^{264}Fm isotope undergoes symmetric fission into two ^{132}Sn nuclei. Hence, this process can be described in the 2D collective space spanned by the deformation coordinates (β_{20},β_{22}). The description of the asymmetric spontaneous fission of ^{250}Fm, on the other hand, necessitates the inclusion of the octupole (reflection-asymmetric) degree of freedom β_{30} and, in principle, calculations should be carried out in the full 3D collective space spanned by the deformation coordinates $(\beta_{20},\beta_{22},\beta_{30})$. In our case this is computationally too demanding and, therefore, the dynamic fission path of ^{250}Fm is constructed from two segments: i) the path that connects the inner turning point and the isomeric state is calculated by minimizing the fission action integral in the (β_{20},β_{22}) plane, and ii) the path between the isomeric state and the outer turning point is determined in the (β_{20},β_{30}) plane. The collective inertia tensors are calculated using the ATDHFB method both in the perturbative and nonperturbative cranking approximations.

Our study has confirmed previous results related to the perturbative approach to modeling the ATDHFB collective inertia tensor. The perturbative treatment underestimates the effects of structural changes at the level crossing at which the nucleus changes its microscopic configuration diabatically, and the resulting collective inertia $\mathcal{M}^{Cp}$ varies relatively smoothly in the (β_{20},β_{22}) and (β_{20},β_{30}) planes. In contrast to the featureless behavior of $\mathcal{M}^{Cp}$, the nonperturbative collective inertia $\mathcal{M}^{C}$ is characterized by the occurrence of sharp peaks on the surface of collective coordinates, that can be related to single-particle level crossings near the Fermi surface, that is, to abrupt changes of occupied single-particle configurations. This leads to an enhancement of the effective inertia, increases the fission action integral, and the resulting half-lives are longer. Consistent results have been obtained using the relativistic energy density functionals PC-PK1 and DD-PC1.

In the case of asymmetric fission of ^{250}Fm we have analyzed the effect of triaxiality in the region around the inner fission barrier. Several recent studies have pointed out that nonaxial shapes are also relevant for the description of outer fission barriers in the actinides [33,49], and this will present an interesting topic for future applications of the model and computing methods developed in this work. An even more important issue is the inclusion of the particle-number fluctuation degree of freedom and the analysis of its impact on SF half-lives. Several recent studies have shown that pairing correlations should be treated on the same footing as shape deformation degrees of freedom, and we have also initiated work along these lines.

ACKNOWLEDGMENTS

This work has been supported in part by the NEWFELPRO project of the Ministry of Science, Croatia, co-financed through the Marie Curie FP7-PEOPLE-2011-COFUND program, and by the Croatian Science Foundation—project "Structure and Dynamics of Exotic Femtosystems" (IP-2014-09-9159). We thank Jhilam Sadhukhan for very helpful discussions. Calculations have been performed in part at the High-performance Computing Cluster of SKLTP/ITP-CAS.

APPENDIX: DYNAMIC-PROGRAMMING METHOD AND RITZ METHOD

This Appendix contains a brief description of the two methods used to find the minimum action path in a two-dimensional collective space, for instance, on the $\beta_{20} \equiv q_0$, $\beta_{22} \equiv q_2$ plane. Two locations are fixed on the path: the inner turning point (q_0^{in}, q_2^{in}) and the outer turning point (q_0^{out}, q_2^{out}).

The Ritz method (RM) [27] is based on the variational procedure. The following ansatz is assumed for the path:

$$q_2(q_0) = \sum_{k=1}^{N} a_k \sin(k\pi x) + f(x), \tag{A1}$$

where the variable x is defined:

$$x = \frac{q_2 - q_2^{in}}{q_2^{out} - q_2^{in}}, \quad 0 \leqslant x \leqslant 1. \tag{A2}$$

The "boundary condition function" $f(x)$ ensures that the path passes through the inner and the outer turning points, and in practical calculations a straight line can be used

$$f(x) = f_0 + (f_1 - f_0)x, \tag{A3}$$

with $f_1 = f(1)$ and $f_0 = f(0)$. The variational parameters a_k are determined to minimize the action integral calculated for the path defined in Eq. (A1). We note that the convergence of the Ritz method is rather fast, already with $N = 10$ stable results are obtained.

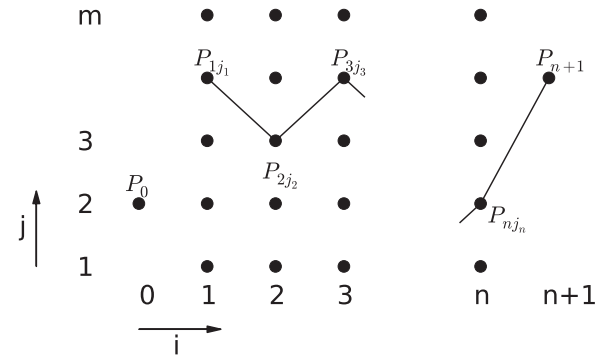

FIG. 13. Schematic diagram of the determination of the optimal trajectory using the dynamic-programming method.

The dynamic-programming method (DPM) [28] uses an equidistant mesh in the plane of collective coordinates, as shown in Fig. 13. The inner and outer turning points are denoted with P_0 and P_{n+1}, respectively, and the path consists of straight line segments connecting the mesh points P_{ij}. In the first step one determines the optimal paths connecting the inner turning point P_0 and each point in the second column of the mesh P_{2j_2} $(j_2 = 1, \ldots, m)$. This is achieved by comparing the action integrals for m paths passing through separate points P_{1j_1} in the first column of the mesh and, in this way, for each point in the second column P_{2j_2} an optimal trajectory is obtained which minimizes the action integral. In the second step the optimal path from the inner turning point P_0 to each point in the third column P_{3j_3} $(j_2 = 1, \ldots, m)$ is determined, again by comparing only m paths passing through various points in the second column P_{2j_2}. This procedure is repeated until the outer turning point is reached, that is, the entire optimal path is constructed. The main advantage of this method is that one has to calculate and compare only $m \times n$ paths from the m^n possible paths on the mesh. The following values for the mesh size have been used in the present analysis: 0.01 for the coordinate β_{20}, 0.001 for β_{22}, and 0.002 for β_{30}.

[1] H. J. Krappe and K. Pomorski, *Theory of Nuclear Fission*, Lecture Notes in Physics Vol. 838 (Springer Verlag, New York, 2012).
[2] P. G. Reinhard and K. Goeke, Rep. Prog. Phys. **50**, 1 (1987).
[3] H. Goutte, J. F. Berger, P. Casoli, and D. Gogny, Phys. Rev. C **71**, 024316 (2005).
[4] W. Younes and D. Gogny, Lawrence Livermore National Laboratory, Tech. Rep. LLNL-TR-586678 (2012).
[5] J. Berger, M. Girod, and D. Gogny, Comput. Phys. Commun. **63**, 365 (1991).
[6] J. Berger, M. Girod, and D. Gogny, Nucl. Phys. A **428**, 23 (1984).
[7] P. Ring and P. Schuck, *The Nuclear Many-Body Problem* (Springer Verlag, New York, 1980).
[8] J. Dobaczewski and J. Skalski, Nucl. Phys. A **369**, 123 (1981).
[9] M. Baranger and M. Véneroni, Ann. Phys. (NY) **114**, 123 (1978).
[10] M. J. Giannoni and P. Quentin, Phys. Rev. C **21**, 2060 (1980).
[11] J. W. Negele, Nucl. Phys. A **502**, 371 (1989).
[12] J. Skalski, Phys. Rev. C **77**, 064610 (2008).
[13] H. Zhang, H. Zhang, J. Li, X. Bao, and N. Ma, Phys. Rev. C **90**, 054313 (2014).
[14] X. Bao, H. Zhang, G. Royer, and J. Li, Nucl. Phys. A **906**, 1 (2013).
[15] P. Möller, J. Nix, and W. Swiatecki, Nucl. Phys. A **492**, 349 (1989).
[16] M. Warda and J. L. Egido, Phys. Rev. C **86**, 014322 (2012).
[17] M. Warda, J. L. Egido, L. M. Robledo, and K. Pomorski, Phys. Rev. C **66**, 014310 (2002).

[18] A. Staszczak, A. Baran, and W. Nazarewicz, Phys. Rev. C **87**, 024320 (2013).
[19] A. Staszczak, A. Baran, J. Dobaczewski, and W. Nazarewicz, Phys. Rev. C **80**, 014309 (2009).
[20] J. Erler, K. Langanke, H. P. Loens, G. Martínez-Pinedo, and P.-G. Reinhard, Phys. Rev. C **85**, 025802 (2012).
[21] N. Schindzielorz, J. Erler, P. Klupfel, P. Reinhard, and G. Hager, Int. J. Mod. Phys. E **18**, 773 (2009).
[22] J.-F. Berger, L. Bitaud, J. Dechargé, M. Girod, and K. Dietrich, Nucl. Phys. A **685**, 1 (2001).
[23] S. A. Giuliani and L. M. Robledo, Phys. Rev. C **88**, 054325 (2013).
[24] R. Rodríguez-Guzmán and L. Robledo, Eur. Phys. J. A **50**, 142 (2014).
[25] M. Brack, J. Damgaard, A. S. Jensen, H. C. Pauli, V. M. Strutinsky, and C. Y. Wong, Rev. Mod. Phys. **44**, 320 (1972).
[26] T. Ledergerber and H.-C. Pauli, Nucl. Phys. A **207**, 1 (1973).
[27] A. Baran, Phys. Lett. B **76**, 8 (1978).
[28] A. Baran, K. Pomorski, A. Lukasiak, and A. Sobiczewski, Nucl. Phys. A **361**, 83 (1981).
[29] S. G. Nilsson, C. F. Tsang, A. Sobiczewski, Z. Szymanski, S. Wycech, C. Gustafson, I.-L. Lamm, P. Moller, and B. Nilsson, Nucl. Phys. A **131**, 1 (1969).
[30] M. Girod and B. Grammaticos, Nucl. Phys. A **330**, 40 (1979).
[31] D. Bés and Z. Szymański, Nucl. Phys. **28**, 42 (1961).
[32] A. Sobiczewski, Z. Szymański, S. Wycech, S. G. Nilsson, J. R. Nix, C. F. Tsang, C. Gustafson, P. Möller, and B. Nilsson, Nucl. Phys. A **131**, 67 (1969).
[33] B.-N. Lu, J. Zhao, E.-G. Zhao, and S.-G. Zhou, Phys. Rev. C **89**, 014323 (2014).
[34] R. Gherghescu, J. Skalski, Z. Patyk, and A. Sobiczewski, Nucl. Phys. A **651**, 237 (1999).
[35] R. Smolańczuk, H. V. Klapdor-Kleingrothaus, and A. Sobiczewski, Acta Phys. Pol. B **24**, 685 (1993).
[36] R. Smolańczuk, J. Skalski, and A. Sobiczewski, Phys. Rev. C **52**, 1871 (1995).
[37] Z. Łojewski and A. Staszczak, Nucl. Phys. A **657**, 134 (1999).
[38] L. Moretto and R. Babinet, Phys. Lett. B **49**, 147 (1974).
[39] A. Staszczak, A. Baran, K. Pomorski, and K. Böning, Phys. Lett. B **161**, 227 (1985).
[40] A. Staszczak, S. Piłat, and K. Pomorski, Nucl. Phys. A **504**, 589 (1989).
[41] S. A. Giuliani, L. M. Robledo, and R. Rodriguez-Guzman, Phys. Rev. C **90**, 054311 (2014).
[42] J. Sadhukhan, J. Dobaczewski, W. Nazarewicz, J. A. Sheikh, and A. Baran, Phys. Rev. C **90**, 061304 (2014).
[43] M. Urin and D. Zaretsky, Nucl. Phys. **75**, 101 (1966).
[44] Y. A. Lazarev, Phys. Scr. **35**, 255 (1987).
[45] K. Pomorski, Int. J. Mod. Phys. E **16**, 237 (2007).
[46] A. Baran, Z. Łojewski, K. Sieja, and M. Kowal, Phys. Rev. C **72**, 044310 (2005).
[47] A. Baran, J. A. Sheikh, J. Dobaczewski, W. Nazarewicz, and A. Staszczak, Phys. Rev. C **84**, 054321 (2011).
[48] J. Sadhukhan, K. Mazurek, A. Baran, J. Dobaczewski, W. Nazarewicz, and J. A. Sheikh, Phys. Rev. C **88**, 064314 (2013).
[49] B.-N. Lu, E.-G. Zhao, and S.-G. Zhou, Phys. Rev. C **85**, 011301(R) (2012).
[50] B.-N. Lu, J. Zhao, E.-G. Zhao, and S.-G. Zhou, EPJ Web Conf. **38**, 05003 (2012).
[51] B.-N. Lu, J. Zhao, E.-G. Zhao, and S.-G. Zhou, J. Phys: Conf. Ser. **492**, 012014 (2014).
[52] B.-N. Lu, J. Zhao, E.-G. Zhao, and S.-G. Zhou, Phys. Scr. **89**, 054028 (2014).
[53] B.-N. Lu, Multi-dimensional constrained relativistic mean field theory and the fission barriers of actinide nuclei, Ph.D. thesis, Institute of Theoretical Physics, Chinese Academy of Sciences, 2012.
[54] J. Zhao, B.-N. Lu, D. Vretenar, E.-G. Zhao, and S.-G. Zhou, Phys. Rev. C **91**, 014321 (2015).
[55] B.-N. Lu, E.-G. Zhao, and S.-G. Zhou, Phys. Rev. C **84**, 014328 (2011).
[56] B.-N. Lu, E. Hiyama, H. Sagawa, and S.-G. Zhou, Phys. Rev. C **89**, 044307 (2014).
[57] J. Zhao, B.-N. Lu, E.-G. Zhao, and S.-G. Zhou, Phys. Rev. C **86**, 057304 (2012).
[58] M. Bender, P.-H. Heenen, and P.-G. Reinhard, Rev. Mod. Phys. **75**, 121 (2003).
[59] D. Vretenar, A. Afanasjev, G. Lalazissis, and P. Ring, Phys. Rep. **409**, 101 (2005).
[60] P. W. Zhao, Z. P. Li, J. M. Yao, and J. Meng, Phys. Rev. C **82**, 054319 (2010).
[61] T. Nikšić, D. Vretenar, and P. Ring, Phys. Rev. C **78**, 034318 (2008).
[62] Y. Tian, Z. Y. Ma, and P. Ring, Phys. Lett. B **676**, 44 (2009).
[63] Y. Gambhir, P. Ring, and A. Thimet, Ann. Phys. (NY) **198**, 132 (1990).
[64] M. J. Giannoni and P. Quentin, Phys. Rev. C **21**, 2076 (1980).
[65] E. Yuldashbaeva, J. Libert, P. Quentin, and M. Girod, Phys. Lett. B **461**, 1 (1999).
[66] A. Baran, A. Staszczak, J. Dobaczewski, and W. Nazarewicz, Int. J. Mod. Phys. E **16**, 443 (2007).
[67] S. Karatzikos, A. Afanasjev, G. Lalazissis, and P. Ring, Phys. Lett. B **689**, 72 (2010).
[68] L. J. Wang, B. Y. Sun, J. M. Dong, and W. H. Long, Phys. Rev. C **87**, 054331 (2013).
[69] A. V. Afanasjev and O. Abdurazakov, Phys. Rev. C **88**, 014320 (2013).
[70] A. Staszczak, A. Baran, and W. Nazarewicz, Int. J. Mod. Phys. E **20**, 552 (2011).